# Oscillating convection and reversal flow in connected cavities

Yue Xiao, Jianjun Tao,* and Xue Ma
*SKLTCS and CAPT-HEDPS, Collaborative Innovation Center of IFSA, Department of Mechanics and Engineering Science, College of Engineering, Peking University, Beijing 100871, P. R. China*

Xiangming Xiong
*School of Mathematics and Statistics, Shenzhen University, Shenzhen 518060, P. R. China*

(Received 16 August 2018; published 20 December 2018)

The two-dimensional natural convection of air in upper and a lower square cavities connected with a vertical vent is studied numerically and theoretically. At high Rayleigh numbers (Ra), it is revealed by the dynamic-mode-decomposition method that the plumes yield to a new sway mode, where the plumes oscillate in the azimuthal direction around the vent ends. In particular, when Ra is high enough, a reversal convection occurs, i.e., the dominating large-scale circulation changes its flow direction quasiperiodically. A van der Pol–type model is developed based on the momentum and the energy equations, and the reversal phenomenon is explained in terms of the relaxation oscillation caused by the competition between the nonlinear advection and the thermal diffusion.

DOI: 10.1103/PhysRevE.98.063109

## I. INTRODUCTION

Buoyancy-induced natural convection in cavities connected with a vertical vent is a simplified model to study the eruptions of hydrothermal vents and volcanoes [1–9], natural ventilation of buildings [10], and passive cooling of electronic components [11]. Early experiments mainly focused on the overall heat and mass transfer rate [12–15], especially the exchange flow rate at the vent and its dependence on the height-to-width aspect ratio of the vent [13,14,16,17]. Three regimes with different flow patterns near the vent were identified in the previous numerical simulations [18–20]. In the conduction regime, there was almost no flow across the vent, where the thermal energy is transferred mainly by conduction. In the countercurrent regime, the flow through the vent is bidirectional, with upflow and downflow each occupying about one half of the vent cross section. In the oscillatory regime, there were sudden bursts of upflow and downflow with well-defined frequencies, whose dependence on the aspect ratio of the vent was numerically investigated [21–24]. In the previous experiments and numerical simulations, the buoyancy driving forces were mostly transient, such as the concentration difference in the brine-water system and the temperature difference of fluid in adiabatic cavities, and could not support a statistically steady state. It is known that the convection structures in a cavity varies with the Rayleigh number [25–27] and have different scales, e.g., the small-scale thermals and the large-scale circulations (LSCs) [28,29]; however, our understanding on the correspondence between the multiscale structures and the character frequencies in the connected cavities at different Rayleigh numbers is still rudimentary.

The buoyancy-driven flow heated from below and cooled from above (e.g., Rayleigh-Bénard convection) has an important feature, i.e., LSC in turbulent regime [30] may change the circulation direction to its opposite stochastically or flow reversal [31–34]. For details we refer to the review paper [35]. This interesting phenomenon has certain similarities with the wind direction of the atmosphere and the magnetic polarity in stars and planets [36,37]. Sugiyama *et al.* [38] analyzed the LSC reversals in a cavity experimentally and numerically, and they mapped out the reversal region in the Rayleigh number–Prandtl number space. The growth of corner rolls was found to play a crucial role for the LSC reversal and was investigated in a number of numerical and experimental studies of the 2D or quasi-2D systems [39–44]. In addition, the proper orthogonal decomposition method was utilized to extract the coherent structures and three principal modes were identified [45]. In order to capture the distinct features of LSC, several stochastic models have been proposed [32,46–49], where the noise-induced switchings of LSC direction, the viscous dissipation in the boundary layers near the walls, and the interaction between the small scale turbulent fluctuations and the large-scale circulations were considered. Low-dimensional deterministic models were developed as well and the ordinary differential equations were derived by remaining some relevant aspects of the Navier-Stokes equations and had chaotic solutions. One model [50] assumed that LSC was strong enough to transfer a plume to the side wall and then the buoyancy counteracted the prevailing flow. Another model [51] was based on an analytical solution of the Boussinesq equations in the inviscid and unforced limit, illustrating that the boundary layers and plumes were not necessary for the LSC reversals. Different from these pioneering studies on the typical Rayleigh-Bénard convection, where thermals and plumes may be formed at any place near the top and bottom boundaries, in this paper the heat (cold) source of the upper (the lower) cavity is fixed

*jjtao@pku.edu.cn

 

at the central vent. By using this simplified configuration and increasing the Rayleigh number gradually, it becomes convenient to explore the initial mechanism governing the reversal phenomenon.

## II. PHYSICAL MODEL AND METHODS

We study the two-dimensional natural convection of air in a closure composed of two identical square cavities with hight $H = 0.2$ m, which are connected with a vertical vent of width $W_t = 10$ mm and height $H_t = 3$ mm. The sidewall temperatures of the upper and the lower cavities are kept at $T_c = 293$ K and $T_h = T_c + \Delta T$, respectively, where $\Delta T$ is the constant temperature difference, representing a persistent buoyancy source. The sidewalls of the vent are adiabatic, and no-slip boundary conditions are applied on all walls. The governing parameters are the Prandtl number $\mathrm{Pr} = \nu/\alpha$ and the Rayleigh number $\mathrm{Ra} = g\beta\Delta T(2H)^3/(\alpha\nu)$, where $\nu$, $\alpha$, and $\beta$ are the kinematic viscosity, the thermal diffusivity, and the thermal expansion coefficient of air at the temperature $T_m = (T_c + T_h)/2$, respectively. $g$ is the magnitude of the gravitational acceleration. The Nusselt number is defined as $\mathrm{Nu} = |2Hq/[k(T_{\mathrm{wall}} - T_m)]|$, where $q$ is the mean heat flux at the corresponding wall with temperature $T_{\mathrm{wall}}$ and $k$ is the thermal conductivity at $T_m$. The temporally averaged Nusselt number is labeled as $\overline{\mathrm{Nu}}$.

In the numerical simulations, air is treated as an ideal gas. The temperature dependencies of its physical parameters (e.g., viscosity and thermal diffusivity) follow the NIST database and the two-dimensional governing equations are

$$\partial_t \rho^* + \nabla \cdot (\rho^* \boldsymbol{u}^*) = 0, \tag{1}$$

$$\partial_t (\rho^* \boldsymbol{u}^*) + \nabla \cdot (\rho^* \boldsymbol{u}^* \boldsymbol{u}^*) = \rho^* \boldsymbol{g} + \nabla P, \tag{2}$$

$$\partial_t (\rho^* C_p T^*) + \nabla \cdot (\rho^* C_p \boldsymbol{u}^* T^*) = \nabla (k \nabla T^*), \tag{3}$$

$$p^* = \rho^* R T^*, \tag{4}$$

where $P = -p^* \boldsymbol{I} + 2\mu(S^* - \frac{1}{3}\boldsymbol{I}\nabla \cdot \boldsymbol{u}^*)$, $S^*$ is the tensor of strain rate, $\mu = \rho\nu$, and $*$ indicates the dimensional variables. These governing equations are solved with FLUENT. The second-order upwind scheme is used for the spatial discretizations of the gradient terms and the second-order implicit scheme is used for the temporal discretization. The body force weighted scheme is used for the interpolation of pressure, and the PISO algorithm is applied for the pressure-velocity coupling. The present numerical schemes are validated by calculating the critical Rayleigh number of the two-dimensional Rayleigh-Bénard convection between two stress-free boundaries with a relative error of 0.65% in comparison with the theoretical prediction [52]. Consequently, the present numerical method is validated to be applicable to simulate the initial stage of transition. In the temperature range studied in this paper, the Prandtl number is 0.7 and its variation with temperature is too small to be considered. For the present model, a coarse grid (65 118 triangular cells) and a fine grid (279 836 triangular cells) are compared in a simulation with $\Delta T = 30$ K, and the relative error of the temperatures measured at the vent center is 0.03%. Therefore, the coarse grid with 65 118 cells with a minimum mesh size of $0.001H$ is used in the following simulations. In addition, the time step of 0.005 s is tested to be small enough to grasp the unsteady behaviors of the convection.

In the following sections, dominating frequencies are obtained first by spectral analysis, and the spatiotemporal evolutions of the corresponding temperature and vorticity structures are obtained with the dynamic mode decomposition (DMD) method [53,54]. DMD is able to identify the dynamic modes and each mode is associated with a defined oscillation frequency and a growth rate. Consider a sequence of snapshots,

$$\boldsymbol{V}_i^j = [v_i, v_{i+1}, \ldots, v_k, \ldots, v_{j-1}, v_j]^H, \tag{5}$$

where $v_k$ stands for the $k$th flow field and the superscript $H$ denotes the conjugate transpose. In order to avoid aliasing and possibly a diverged decomposition, the above snapshots must be sampled at a sufficiently high frequency. It is assumed that the flow field $v_k$ and the subsequent flow field $v_{k+1}$ are connected by a linear mapping $\boldsymbol{A}$, and the goal of DMD is to extract the dynamic characteristics (eigenvalues, eigenvectors, etc.) of the linear operator $\boldsymbol{A}$,

$$\boldsymbol{A}\boldsymbol{V}_1^{N-1} = \boldsymbol{V}_2^N. \tag{6}$$

Robustness is achieved by a preprocessing step using a singular value decomposition of the data sequence $\boldsymbol{V}_1^{N-1} = \boldsymbol{U}\boldsymbol{\Sigma}\boldsymbol{W}^H$, where $\boldsymbol{U}$ and $\boldsymbol{W}$ are unitary matrices. Considering a similarity transformation

$$\boldsymbol{S} = \boldsymbol{U}^H \boldsymbol{A} \boldsymbol{U} = \boldsymbol{U}^H \boldsymbol{V}_2^N \boldsymbol{W} \boldsymbol{\Sigma}^{-1}, \tag{7}$$

whose right-hand side term is known, we can get the eigenvalue $e_i$ of $\boldsymbol{S}$, $\boldsymbol{S}\boldsymbol{y}_i = e_i \boldsymbol{y}_i$, $1 \leqslant i \leqslant N-1$. Consequently, the eigenvector or the dynamic mode $\boldsymbol{\Phi}_i$ of $\boldsymbol{A}$ can finally be obtained as

$$\boldsymbol{\Phi}_i = \boldsymbol{U}\boldsymbol{y}_i. \tag{8}$$

The corresponding frequency and growth rate of the dynamic mode $\boldsymbol{\Phi}_i$ are the imaginary part and the real part of $\lambda_i$, where $\lambda_i = \log e_i/\Delta t$ and $\Delta t$ is the sampling time. It is verified that $\Delta t = 0.2$s is small enough to capture the key features of the flow and is used in the following data analyses.

## III. DEVELOPMENT OF OSCILLATION

With the increase of Rayleigh number, different flow patterns are shown by the streamlines and the isotherms in Fig. 1. When Rayleigh number is sufficiently small, the vertical velocity at the horizontal midline of the vent is negligible, and there is almost no flow across the vent. Heat exchange between the cavities is achieved mainly by conduction. The vent provides a localized bottom heat source for the upper cavity and a localized top cooling source for the lower cavity. A pair of countercirculating cells therefore emerge in each cavity, and the whole flow pattern is symmetric about the vertical midline. Similar symmetric structures have been observed before [18–20,55–59]. The flow pattern at higher Ra can be obtained efficiently by using the flow field of lower Ra as the initial one. It is shown in Fig. 1 that the flow structure deviates slightly from the symmetric as Ra increases to $1.58 \times 10^8$ but changes qualitatively at $\mathrm{Ra} = 1.95 \times 10^8$ ($\Delta T = 40$ K), where symmetry breaking occurs for the circulation pair in the lower cavity: one becomes larger and the other breaks into two small corner vortices. The circulations in the upper

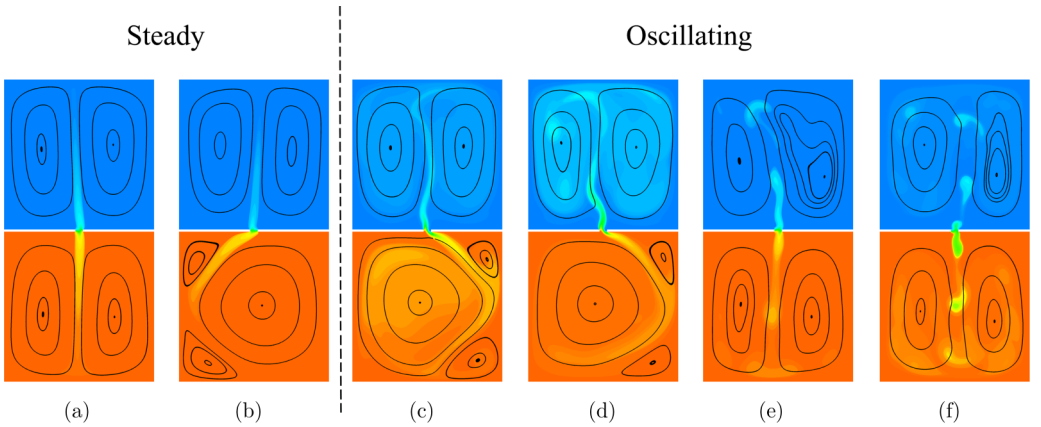


FIG. 1. Transient flow patterns shown by streamlines (black lines) and isotherms in the partitioned cavity at Rayleigh numbers Ra = $1.58 \times 10^8$, $1.95 \times 10^8$, $2.19 \times 10^8$, $2.27 \times 10^8$, $2.53 \times 10^8$, $2.75 \times 10^8$ in (a)–(f), respectively.

cavity do not change significantly and the whole flow field is still steady. It should be noted that the dominating large-scale circulation in the lower cavity may be close to either vertical sidewall depending on the initial field, and the flow pattern is not necessary to be symmetric about the horizontal midplane of the vent because the fluid is assumed to be an ideal gas with temperature-dependent physical properties.

### A. 2-1 Bioscillating convection ($\Delta T = 47$ K, Ra = $2.19 \times 10^8$)

When the Rayleigh number is increased to $2.19 \times 10^8$, the steady hot plume in the upper cavity becomes unstable to an sinuously oscillating mode as shown in Fig. 1(c) and the temporal variations of signals are shown in Fig. 2(a). The flow is referred to as bioscillating convection because there are two characteristic frequencies according to the power spectrum of the temperature measured at the vent center [Fig. 2(b)], i.e., $f_1 = 0.639$ Hz and $f_2 = 0.136$ Hz. DMD analyses are carried out for the temperature and vorticity fields, and the corresponding flow structure of each frequency is revealed. DMD mode with frequency $f_0 = 0$ represents the averaged field, whose pattern is similar to that of the steady state at Ra = $1.95 \times 10^8$ (Fig. 1). It is shown by the middle column of Fig. 3 that the localized temperature and vortex structures

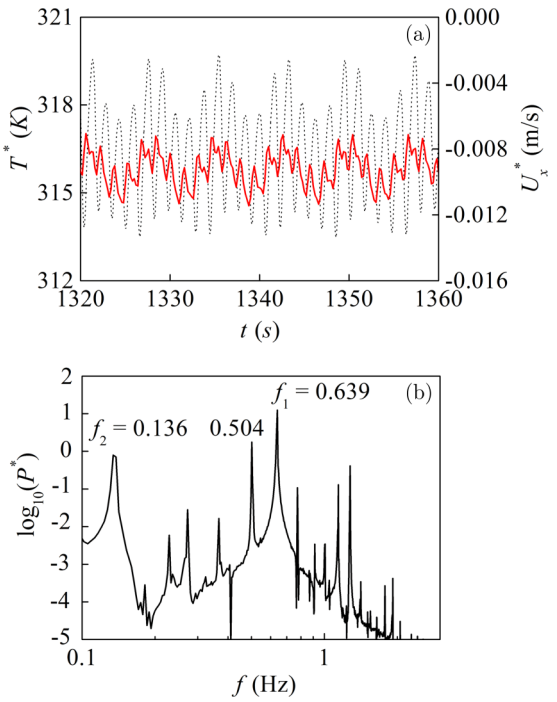


FIG. 2. (a) Time series of velocity (solid line) and temperature (dash line) measured at the vent center for Ra = $2.19 \times 10^8$ and (b) the corresponding power spectrum of temperature calculated based on the data between $t = 1300$ s and 1400 s.

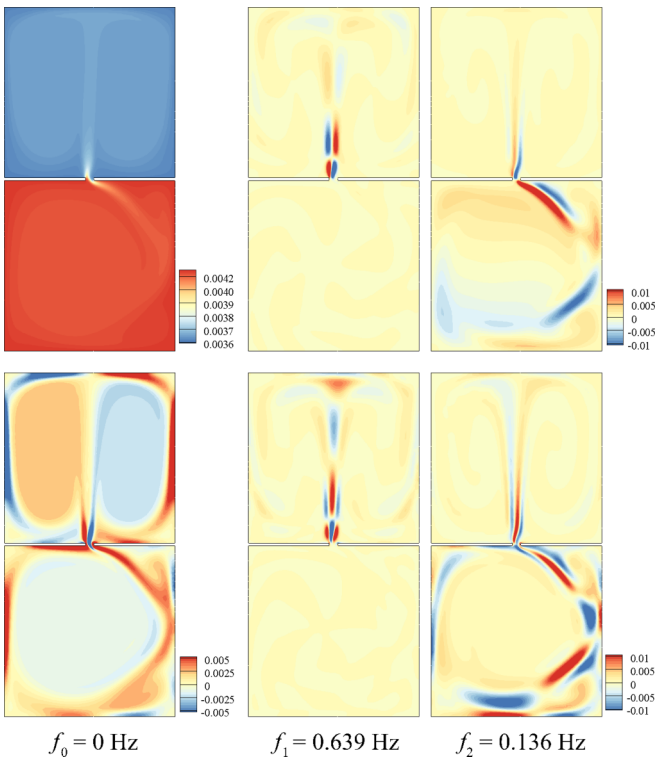


FIG. 3. Isocontours of DMD dynamic modes for Ra = $2.19 \times 10^8$ obtained within the time interval 1400–1420 s with 101 snapshots. The top and the bottom rows correspond to the temperature and the vorticity fields, respectively, and the related frequency is labeled at the bottom of each column.

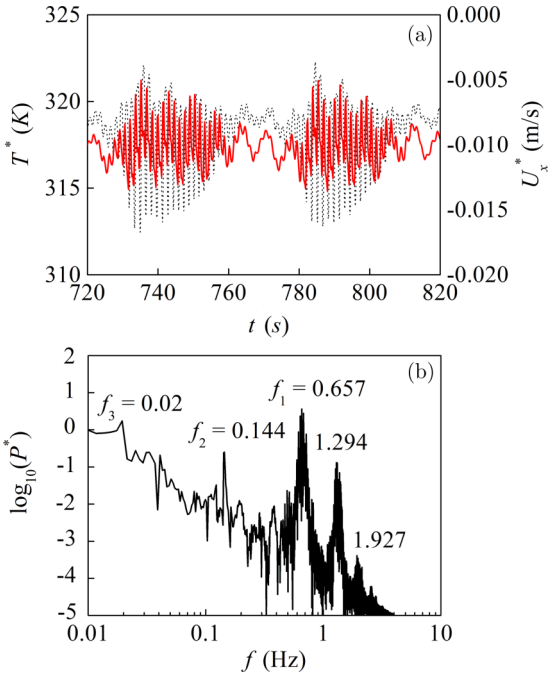


FIG. 4. (a) Time series of velocity (solid line) and temperature (dash line) measured at the vent center for Ra $= 2.27 \times 10^8$ and (b) the corresponding power spectrum of temperature calculated based on the data between $t = 600$ s and 920 s.

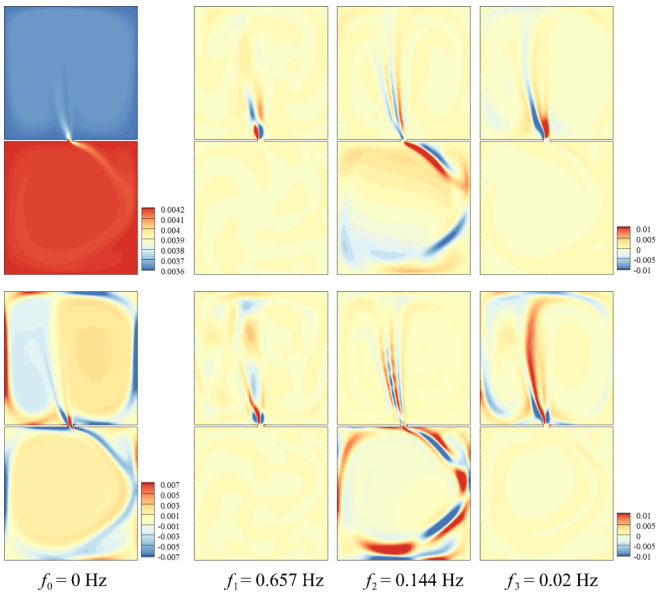


FIG. 5. Isocontours of DMD dynamic modes for Ra $= 2.27 \times 10^8$ obtained within the time interval 575–625 s with 251 snapshots. The top and the bottom rows correspond to the temperature and the vorticity fields, respectively, and the related frequency is labeled at the bottom of each column.

of $f_1$ in the upper cavity correspond to the short-wavelength plume near the vent. Different from the structure of $f_1$, the DMD mode of $f_2$ mainly reflects the large-scale circulation at the lower cavity as shown in the right column of Fig. 3. Another frequency, 0.504 Hz, is close to the difference between these two characteristic frequencies, representing the nonlinear interaction between the hot plume and the LSC in the connected cavities. Considering that there are two LSCs in the upper cavity and one in the lower cavity, the flow field at Ra $= 2.19 \times 10^8$ is named as 2-1 bioscillating convection hereafter.

### B. 2-1 Trioscillating convection ($\Delta T = 50$ K, Ra $= 2.27 \times 10^8$)

The transient flow patterns at Ra $= 2.27 \times 10^8$ look similar to those of Ra $= 2.19 \times 10^8$ as shown in Fig. 1, but LSCs in the upper cavity become asymmetric about the vertical middle line: One becomes dominating and the other turns to be narrow. Furthermore, there are three characteristic frequencies according to the time series of the temperature (Fig. 4). In comparison with the 2-1 bioscillating convection (e.g., Ra $= 2.19 \times 10^8$), the character frequencies of the short-wavelength mode in the upper cavity and of the LSC in the lower cavity increase slightly from 0.639 and 0.136 Hz to 0.657 and 0.144 Hz, respectively. A new or the third character frequency, $f_3 = 0.02$ Hz, appears and corresponds mainly to a sway mode of the hot plume in the upper cavity as shown by the right column of Fig. 5. It is noted that the sway mode with very low (the third) frequency or very long period has not been reported before because the thermal boundary conditions used in the previous studies are different from the present model and cannot provide persistent driven force for the convection.

The mechanism of the sway oscillation may be explained as follows. When the mirror symmetry of the mean flow about the vertical middle line in the upper cavity is broken and one circulation is bigger than the other, the temperature difference

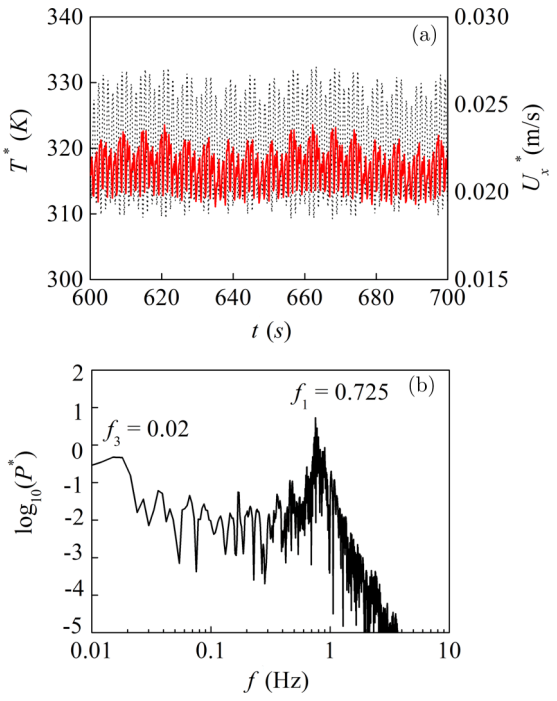


FIG. 6. (a) Time series of velocity (solid line) and temperature (dash line) measured at the vent center for Ra $= 2.53 \times 10^8$ and (b) the corresponding power spectrum of temperature calculated based on the data between $t = 560$ s and 720 s.

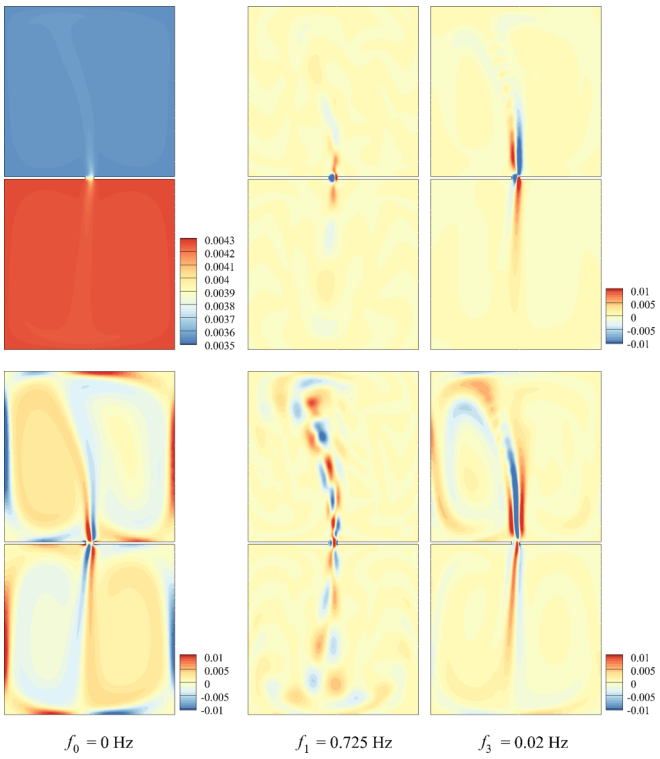


FIG. 7. Isocontours of DMD dynamic modes for Ra = 2.53 × $10^8$ obtained within the time interval 620–670 s with 251 snapshots. The top and the bottom rows correspond to the temperature and the vorticity fields, respectively, and the related frequency is labeled at the bottom of each column.

between the left and the right parts of the cavity will be accumulated due to the asymmetric energy transportation of LSCs. On the other hand, thermal diffusion tends to diminish this temperature difference, and hence it is the LSCs' competition or more intrinsically the dynamic competition between the thermal diffusion and the nonlinear advection that leads to the low-frequency sway of the plume. Considering that there are two circulations in the upper cavity and one in the lower, the convection is called 2-1 trioscillating convection. Similarly to the 2-1 bioscillating convection, DMD modes of $f_1$ and $f_2$ mainly reflect the short-wavelength plume components in the upper cavity and the LSC in the lower cavity (Fig. 5), respectively. It should be noted that with the increase of Ra, the nonlinear effect becomes strong and the harmonic frequencies of the first frequency appear [Fig. 4(b)].

### C. 2-2 Oscillating convection ($\Delta T$ = 60 K, Ra = 2.53 × $10^8$)

A dramatic change of the flow pattern occurs when Ra increases to 2.53 × $10^8$, where the single LSC in the lower cavity becomes two large counter-rotating ones, and hence the flow is named 2-2 oscillating convection. The contribution of the second frequency 0.173 Hz to the power spectrum becomes weak, and the temperature signal at the vent center is characterized by the first frequency 0.725 Hz and the third frequency 0.02 Hz as shown in Fig. 6. The mean-field patterns shown by DMD mode of $f_0 = 0$ Hz in Fig. 7 are nearly antisymmetric about the horizontal middle line.

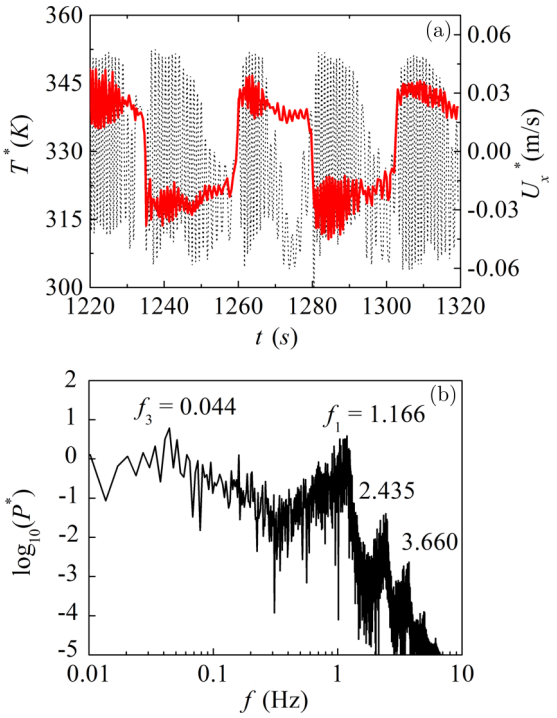


FIG. 8. (a) Time series of velocity (solid line) and temperature (dash line) measured at the vent center for Ra = 2.75 × $10^8$ and (b) the corresponding power spectrum of temperature calculated based on the data between $t$ = 1200 s and 1500 s.

It is noted that the plumes include now two kinds of motions, the short-wavelength sinuous oscillation and the plume sway. The upward hot plume and the downward cold plume break into small-scale thermals at some downstream positions [Fig. 1(e)], which correspond to the first frequency as shown by the dynamic mode of vorticity in Fig. 7. The DMD mode of $f_3 = 0.02$ Hz reflects clearly the plume's azimuthal sway about the central vent, a phenomenon similar to the 2-1 trioscillating convection. In addition, the power spectrum of the temperature series has become continuous as shown in Fig. 6(b), indicating that the flow turns to be chaotic.

### D. Reversal convection ($\Delta T$ = 70 K, Ra = 2.75 × $10^8$)

When Rayleigh number is increased further, it is shown in Fig. 1 (Ra = 2.75 × $10^8$) that the upward and downward thermals are formed alternately near the vent. Different from the earlier convection stages (e.g., 2-1 trioscillating and 2-2 oscillating convections) where the plume in the upper cavity sways but always tilts to one side, when Ra is as high as 2.75 × $10^8$ the plume changes its tilt direction quasiperiodically. Consequently, the direction of the dominating large-scale circulation overturns from time to time or the reversal convection occurs. When one circulation is larger than its neighbor, the horizontal velocity $U_x^*$ at the vent center will deviate from zero. It is shown in Fig. 8(a) that $U_x^*$ changes its sign quasiperiodically, reflecting the reversal process. The large-period oscillation of $U_x^*$ corresponds to the third frequency observed in the earlier stages. Note that one $U_x^*$ reversal includes two periods of strong temperature perturbations [Fig. 8(a)], and hence the corresponding frequency for the

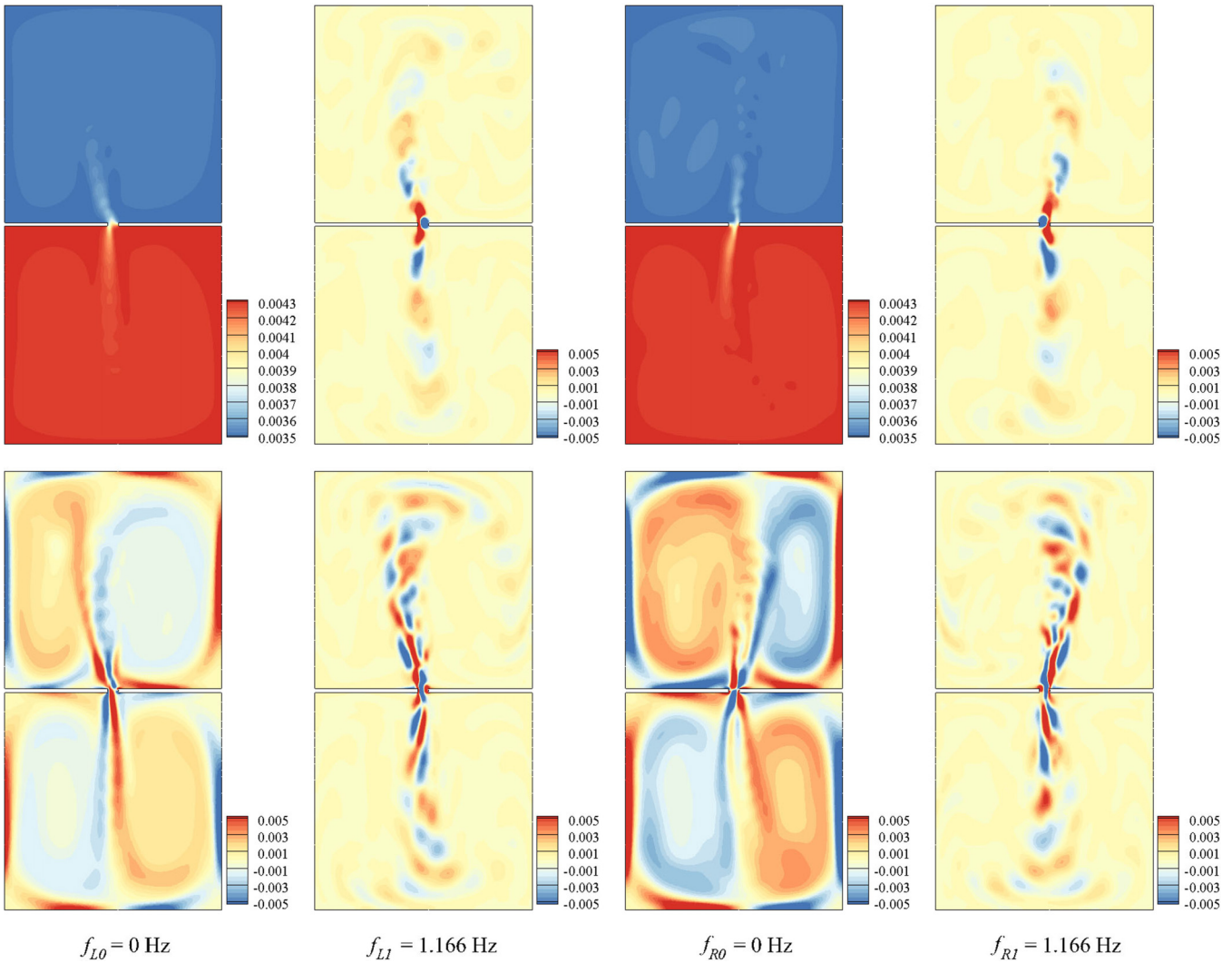


FIG. 9. Isocontours of DMD dynamic modes for Ra = $2.75 \times 10^8$. The left two columns are obtained within 1460–1470 s with 51 snapshots, and the right two columns are based on 1440–1450 s with 51 snapshots. The top and the bottom rows correspond to the temperature and the vorticity fields, respectively, and the related frequency is labeled at the bottom of each column.

reversal convection shown by the temperature power spectrum is 0.044 Hz [Fig. 8(b)], twice as much as the third frequency. The DMD dynamic modes are calculated according to the data of each half period of the reversal convection. It is shown clearly in Fig. 9 that the thermals formed near the vent are transported by the dominating LSC in each cavity, where the two LSCs alternatively dominate the convection during their corresponding half periods. This reversal phenomenon exists as well when $\Delta T$ is increased to 80 K.

Heat transfer efficiency has a strong correlation with the flow structures. The thermal energy is transferred into the lower cavity and transported to the upper cavity. The time-averaged Nusselt number $\overline{\mathrm{Nu}}$ for the lower and the upper cavities at different Rayleigh numbers are shown in Fig. 10 and are consistent with each other, indicating that the flow reaches its statistical equilibrium states. It should be noted that multisolutions for a given Rayleigh number is possible because of the initial-field effect, and the results of unsteady flows discussed in this paper are obtained by gradually increasing Ra. It is shown in Fig. 10 that at low Ra, the flow is steady and $\overline{\mathrm{Nu}}$ is small. When the symmetry breaking occurs in the lower cavity and a dominating large-scale circulation is formed, the flow becomes unsteady at higher Ras and the

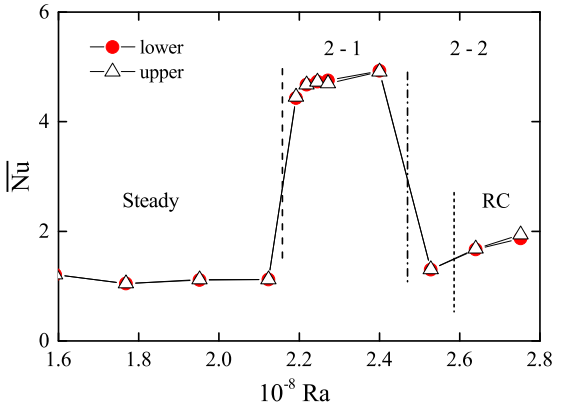


FIG. 10. Time-averaged Nusselt number $\overline{\mathrm{Nu}}$ of the lower and the upper cavities at different Rayleigh numbers.

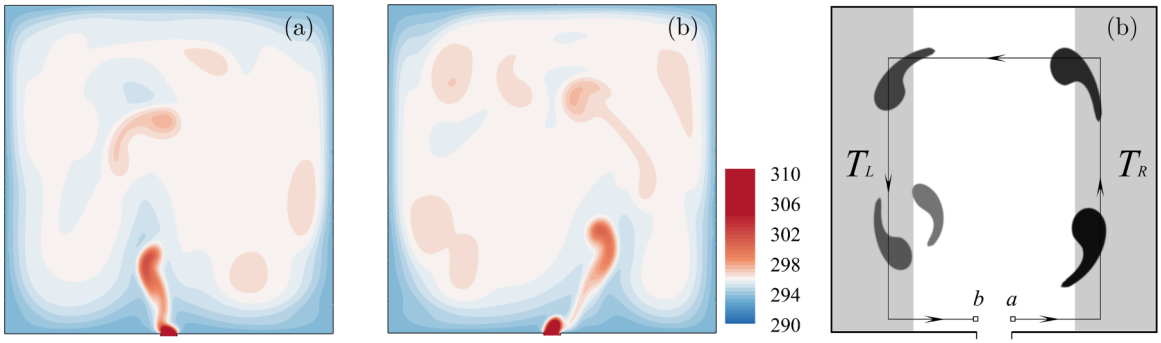


FIG. 11. Transient isothermals indicating (a) the clockwise and (b) the anticlockwise large-scale circulations in the upper cavity at Ra = $2.75 \times 10^8$. (c) Schematic diagram of the physical model.

convective heat transfer is enhanced substantially. However, when the dominating circulation in the lower cavity turns to be two cells at high Ra, e.g., Ra = $2.53 \times 10^8$, the mean vorticity structures of both cavities are nearly antisymmetric about the horizontal middle line of the vent and $\overline{\mathrm{Nu}}$ decreases sharply. Therefore, the heat transfer efficiency of this connected cavities is not a monotonic function of the Rayleigh number.

## IV. MODEL OF REVERSAL CONVECTION

In order to understand the underlying mechanism of the LSC reversal (Fig. 11), we derive a dynamic model based on the momentum equation and the energy equation nondimensionalized with the character length, temperature, and velocity of $H(8\mathrm{Pr}/\mathrm{Ra})^{1/4}$, $\Delta T$, and $\nu[\mathrm{Ra}/(8\mathrm{Pr})]^{1/2}/H$, respectively. For simplicity, we introduce $\mathrm{Gr} = [\mathrm{Ra}/(8\mathrm{Pr})]^{1/4}$ and these two equations become

$$\partial_\tau \boldsymbol{u} + (\boldsymbol{u}\cdot\nabla)\boldsymbol{u} = -\nabla p - \frac{1}{\mathrm{Gr}}\boldsymbol{T} + \frac{1}{\mathrm{Gr}}\Delta\boldsymbol{u}, \tag{9}$$

$$\partial_\tau T + \boldsymbol{u}\cdot\nabla T = \frac{1}{\mathrm{GrPr}}\Delta T, \tag{10}$$

where $\boldsymbol{T}$ is in the same direction of $\boldsymbol{g}$. $l_c$ is the anticlockwise rectangle route of the dominating LSC as shown in Fig. 11(c), and the equations are integrated along $l_c$. For example, the route-mean velocity is defined as $U = \frac{1}{l_c}\int_a^b \boldsymbol{u}\cdot d\boldsymbol{l}$, where $a$ and $b$ are the start and end points of $l_c$ near the top end of the vent. According to Eq. (9), the viscous diffusion is a linear term of $\boldsymbol{u}$ and hence its route-mean value is evaluated as $C_{2a}U/\mathrm{Gr}$. The mean advection term [the second term on the left-hand side of Eq. (9)] should contribute to the dominating LSC in a similar way for both the clockwise and the anticlockwise cases and hence should be an odd function of $U$ and is approximated as $(C_{2b}U + C_1U^3)$. After the integration, the mean pressure term is $P_{ab} = (p_a - p_b)$, the horizontal pressure difference near the vent, mainly reflecting the high-frequency ($\omega$, the dimensionless form of $f_1$) oscillation due to the thermal formation. Considering that the pressure scales as $U^2$, $(p_a - p_b)$ is estimated as $C_3U^2\cos(2\pi\omega\tau)$. Note that the driven force of this convection system is not an externally exerted pressure gradient but the buoyancy, the long-period reversal flow, is not sensitive to the sign of $C_3U^2$, which only affects the initial phase of the high-frequency motion. The horizontal segments of $l_c$ is normal to $\boldsymbol{g}$, and hence the line integration of $-\boldsymbol{T}$ is evaluated as $T_{RL} = C_0(T_R - T_L)$, where $T_R$ and $T_L$ are the averaged temperature in the right and the left gray regions with width of $H/4$ shown in Fig. 11, respectively. From the energy equation [Eq. (10)] we know that $T_{RL}$ is related to the thermal advection and the thermal diffusion, and hence its growth rate should be positively correlated with the ratio of the advection to diffusion or $\mathrm{GrPr}U$. Consequently, we obtain the model equations as

$$\frac{dU}{d\tau} = \frac{C_0}{\mathrm{Gr}}T_{RL} - C_1U^3 + C_2U + C_3U^2\cos(2\pi\omega\tau), \tag{11}$$

$$\frac{dT_{RL}}{d\tau} = C_4\mathrm{GrPr}U, \tag{12}$$

where $C_2 = \frac{1}{\mathrm{Gr}}C_{2a} - C_{2b}$. If we assume $A = 3C_1 = C_2$, $B = -C_0C_4\mathrm{Pr}$, and $C_3 = 0$, then the above model equations turn to be

$$\frac{d^2U}{d\tau^2} + A(U^2 - 1)\frac{dU}{d\tau} + BU = 0. \tag{13}$$

The above equation is van der Pol equation describing relaxation oscillation in nonlinear dynamic systems. The fourth-order Runge-Kutta method with adaptive time step control is used to solve Eqs. (11) and (12). According to the dependence of $U$ and $T_{RL}$ on these coefficients, the $C$s are determined with the coordinate descent method. At first, the high-frequency components are ignored and hence $C_3 = 0$, and the initial values of $C_0$, $C_1$, and $C_2$ are all set to 1. $C_4$ is adjusted to fit the variation amplitude of $T_{RL}$, and $C_0$, $C_2$, and $C_1$ are modulated in turn to fit the reversal period, the variation amplitude of $U$, and the steepness of $U$, respectively. This procedure is iterated, and when the model predictions are fair close to the numerical results $C_3$ is adjusted to fit the amplitude of high-frequency component of $U$. The whole process is iterated to obtain a better approximation. When $(C_0, C_1, C_2, C_3, C_4) = (1.71, 2.5, 0.005, 0.1, -8.3 \times 10^{-7})$, the model solutions are compared with the numerical results at Ra = $2.75 \times 10^8$ with $f_1 = 1.166$ Hz ($\omega = 0.0043$). The reversal mechanism is the same for the upper and the lower cavities and the upper cavity is used as an example. The horizontal velocity $U_x$ at the top center of the vent reflects the circulation velocity of the dominating LSC in the upper cavity. It is shown in Fig. 12(a) that $U_x$ changes its sign abruptly after slow decrease of its amplitude, a key feature of the reversal phenomenon. The temporal evolution of $U_x$ is successfully described by the model, indicating that this kind of reversal convection is

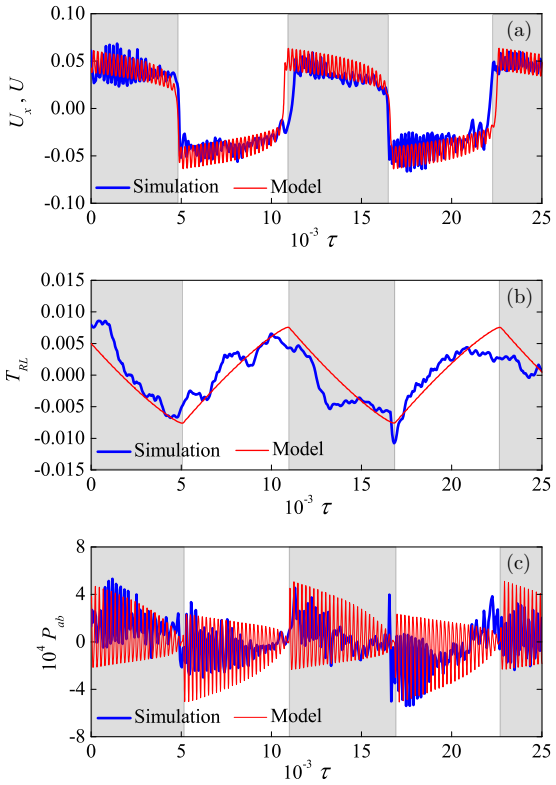


FIG. 12. Comparison of the (a) velocity, (b) temperature difference, and (c) pressure difference between the model and the simulation results in the upper cavity at Ra $= 2.75 \times 10^8$. The horizontal velocity $U_x$ is the simulation value measured at the top center of the vent. $P_{ab} = (p_a - p_b)$ and the pressure $p_a$ and $p_b$ are measured at the points of half-vent height $H_v/2$ above the vent's top edges in simulations. The gray regions indicate the anticlockwise motion of the dominating LSC.

intrinsically related to the relaxation oscillation. In addition, the high-frequency oscillation of $U_x$ caused by the thermal formation becomes weak before the reversal, and this phenomenon is grasped as well by the model. Let us start with an anticlockwise LSC where the velocity at the top center of the vent $U_x$ is positive. The small-scale hot thermals are transported by the LSC and accumulated at the left side of the cavity as shown by the simulation [Fig. 11(b)], leading to the increase of the left mean temperature $T_L$ and the decrease of the right-left temperature difference $T_{RL}$ as illustrated by Fig. 12(b). Because of the inertia, the dominating LSC will not stop as $T_{RL} = 0$ and hence $T_{RL}$ will continue to decrease and turn to be negative, providing a resisting buoyancy force to the circulation. When $T_{RL}$ reaches a threshold, the buoyancy effect reverses the LSC to a clockwise one, $U_x$ becomes negative, and $T_{RL}$ begins to increase until the next reversal. In addition, as shown in Fig. 12(c) the main temporal feature of the pressure difference near the vent top can be described by the model as well. It should be noted that the modeled reversal phenomenon exists even without the high-frequency terms ($C_3 = 0$) in Eq. (11), a behavior similar to that for the van de Pol equation [Eq. (13)]. Therefore, it is suggested that the two-dimensional reversal convection originates from the relaxation oscillation caused by the competition between the advection and the thermal diffusion.

## V. CONCLUSIONS

In this paper the natural convection in two cavities connected with a vertical vent is numerically simulated, and the flow structures at different Rayleigh numbers are analyzed. The wall temperature of each cavity is uniform, and the constant temperature difference between the upper and the lower cavities provides a lasting driven force and makes it possible to study the long-term behaviors of the flow. With the increase of Ra, the convection changes from steady flow to oscillating states, whose key feature is the interaction between small-scale structures and large-scale circulations. The LSCs are driven by plumes originated at the vent ends. The plumes become unstable to short-wavelength sinuous modes with a high frequency ($f_1$) as Ra is large enough and at higher Rayleigh numbers will suffer to an additional sway mode, where the plume oscillates in the azimuthal direction around the vent end with a low frequency ($f_3$). When Ra is increased further, the short-wavelength component breaks into small thermals transported away by LSCs. Because of the dramatic changes of the flow pattern, the Nusselt number is not a monotonic function of Ra.

More importantly, a reversal convection appears as Ra is larger than $2.64 \times 10^8$, where the direction of the dominating LSCs in the cavities is reversed with a low statistical frequency consistent with the sway frequency. Based on the NS equations and the energy equation, a van der Pol–type model is built and it is shown that the reversal phenomenon is successfully described by the relaxation oscillation process caused by the competition between the nonlinear advection and the thermal diffusion. Though the Prandtl number, the aspect ratio of the vent, the compressibility of the fluid, and the turbulent states will affect the characteristics of the reversal flow, the momentum and energy conservation laws are universal, and hence it is believed that the origin of reversal convection should be intrinsically related to the relaxation oscillation as predicted by the model.

## ACKNOWLEDGMENTS

The authors thank Jun Zhang and Hengdong Xi for enlightening discussions on the reversal phenomenon. This work has been supported by the National Natural Science Foundation of China (Grants No. 91752203, No. 11490553, and No. 11521091).

[1] R. F. Weiss, P. Lonsdale, J. E. Lupton, A. E. Bainbridge, and H. Craig, Nature **267**, 600 (1977).

[2] J. B. Corliss, J. Dymond, L. I. Gordon, J. M. Edmond, R. P. von Herzen, R. D. Ballard, K. Green, D. Williams, A. Bainbridge, K. Crane, and T. H. van Andel, Science **203**, 1073 (1979).

[3] F. N. Spiess, K. C. Macdonald, T. Atwater, R. Ballard, A. Carranza, D. Cordoba, C. Cox, V. M. D. Garcia,

J. Francheteau, J. Guerrero, J. Hawkins, R. Haymon, R. Hessler, T. Juteau, M. Kastner, R. Larson, B. Luyendyk, J. D. Macdougall, S. Miller, W. Normark, J. Orcutt, and C. Rangin, Science **207**, 1421 (1980).

[4] H. P. Johnson, M. A. Tivey, T. A. Bjorklund, and M. S. Salmi, Geochem. Geophy. Geosy. **11**, 1 (2010).

[5] A. Tagliabue, L. Bopp, J.-C. Dutay, A. R. Bowie, F. Chever, P. Jean-Baptiste, E. Bucciarelli, D. Lannuzel, T. Remenyi, G. Sarthou, O. Aumont, M. Gehlen, and C. Jeandel, Nat. Geosci. **3**, 252 (2010).

[6] S. E. Beaulieu, E. T. Baker, C. R. German, and A. Maffei, Geochem. Geophy. Geosy. **14**, 4892 (2013).

[7] D. Coumou, T. Driesner, and C. A. Heinrich, Science **321**, 1825 (2008).

[8] J. Hasenclever, S. Theissen-Krah, L. H. Rüpke, J. P. Morgan, K. Iyer, S. Petersen, and C. W. Devey, Nature **508**, 508 (2014).

[9] F. J. Fontaine, M. Rabinowicz, and M. Cannat, Geochem. Geophy. Geosy. **18**, 1907 (2017).

[10] P. F. Linden, Annu. Rev. Fluid Mech. **31**, 201 (1999).

[11] E. Yu and Y. K. Joshi, IEEE Trans. Compon., Packag. Technol. **23**, 14 (2000).

[12] W. G. Brown, Int. J. Heat Mass Tran. **5**, 869 (1962).

[13] M. Epstein, J. Heat Tran. **110**, 885 (1988).

[14] Q. Tan and Y. Jaluria, Flow through horizontal vents as related to compartment fire environments, Tech. Rep. NIST-GCR-92-607, Rutgers University Report to NIST (U.S. National Institute of Standards and Technology, Gaithersburg, MD, 1992).

[15] S. B. Riffat and L. Shao, Build. Serv. Eng. Res. T. **16**, 149 (1995).

[16] T. A. Myrum, Trans. ASME J. Heat Trans-T ASME **112**, 632 (1990).

[17] T. A. Conover, R. Kumar, and J. S. Kapat, J. Heat Tran. **117**, 641 (1995).

[18] M. Singhal and R. Kumar, J. Heat Tran. **117**, 515 (1995).

[19] R. Kumar, A. Sleiti, and J. Kapat, J. Thermophys. Heat Tran. **20**, 276 (2006).

[20] A. A. Mishra, N. Hasan, S. Sanghi, and R. Kumar, Phys. Fluids **20**, 063601 (2008).

[21] R. E. Spall and E. A. Anderson, Numer. Heat Tr. A-appl. **36**, 263 (1999).

[22] R. P. Harrison and R. E. Spall, Numer. Heat Tr. A-appl. **44**, 451 (2003).

[23] B. Gera, P. K. Sharma, R. K. Singh, and K. K. Vaze, CFD Lett. **4**(1), 20 (2012).

[24] B. Gera, P. K. Sharma, and R. K. Singh, Heat Tran. Asian Res. **41**, 666 (2012).

[25] J. Tao, P. Le Quéré, and S. Xin, Phys. Rev. E **70**, 066311 (2004).

[26] S. Xin and P. L. Quéré, Fluid Dyn. Res. **44**, 031419 (2012).

[27] J. Ma, F. Xu, and S. Saha, Int. Commun. Heat Mass Transfer **88**, 220 (2017).

[28] E. M. Sparrow, R. Husar, and R. Goldstein, J. Fluid Mech. **41**, 793 (1970).

[29] J. Zhang and A. Libchaber, Phys. Rev. Lett. **84**, 4361 (2000).

[30] R. Krishnamurti and L. N. Howard, Proc. Natl. Acad. Sci. USA **78**, 1981 (1981).

[31] J. J. Niemela, L. Skrbek, K. R. Sreenivasan, and R. J. Donnelly, J. Fluid Mech. **449**, 169 (2001).

[32] K. R. Sreenivasan, A. Bershadskii, and J. J. Niemela, Phys. Rev. E **65**, 056306 (2002).

[33] E. Brown, A. Nikolaenko, and G. Ahlers, Phys. Rev. Lett. **95**, 084503 (2005).

[34] H. D. Xi, Q. Zhou, and K. Q. Xia, Phys. Rev. E **73**, 056312 (2006).

[35] G. Ahlers, S. Grossmann, and D. Lohse, Rev. Mod. Phys. **81**, 503 (2009).

[36] G. A. Glatzmaiers and P. H. Roberts, Nature **377**, 203 (1995).

[37] S. K. Solanki and N. A. Krivova, Science **334**, 916 (2011).

[38] K. Sugiyama, R. Ni, R. J. A. M. Stevens, T. S. Chan, S.-Q. Zhou, H.-D. Xi, C. Sun, S. Grossmann, K.-Q. Xia, and D. Lohse, Phys. Rev. Lett. **105**, 034503 (2010).

[39] A. Y. Vasil'ev and P. G. Frick, JETP Lett. **93**, 330 (2011).

[40] T. Yanagisawa, Y. Yamagishi, Y. Hamano, Y. Tasaka, and Y. Takeda, Phys. Rev. E **83**, 036307 (2011).

[41] M. Chandra and M. K. Verma, Phys. Rev. E **83**, 067303 (2011).

[42] S. Wagner and O. Shishkina, Phys. Fluids **25**, 085110 (2013).

[43] M. Chandra and M. K. Verma, Phys. Rev. Lett. **110**, 114503 (2013).

[44] S. N. Xia, Z. H. Wan, S. Liu, Q. Wang, and D. J. Sun, J. Fluid Mech. **798**, 628 (2016).

[45] B. Podvin and A. Sergent, J. Fluid Mech. **766**, 172 (2015).

[46] R. Benzi, Phys. Rev. Lett. **95**, 024502 (2005).

[47] E. Brown and G. Ahlers, Phys. Rev. Lett. **98**, 134501 (2007).

[48] E. Brown and G. Ahlers, Phys. Fluids **20**, 075101 (2008).

[49] R. Benzi and R. Verzicco, Europhys. Lett. **81**, 64008 (2008).

[50] F. F. Araujo, S. Grossmann, and D. Lohse, Phys. Rev. Lett. **95**, 084502 (2005).

[51] C. Resagk, R. D. Puits, A. Thess, F. V. Dolzhansky, S. Grossmann, F. F. Araujo, and D. Lohse, Phys. Fluids **18**, 095105 (2006).

[52] S. Chandrasekhar, *Hydrodynamic and Hydromagnetic Stability* (Clarendon Press, Oxford, 1961).

[53] P. J. Schmid, J. Fluid Mech. **656**, 5 (2010).

[54] I. Mezić, Annu. Rev. Fluid Mech. **45**, 357 (2013).

[55] R. Harish and K. Venkatasubbaiah, Comput. Fluids **96**, 276 (2014).

[56] K. E. Torrance, L. Orloff, and J. A. Rockett, J. Fluid Mech. **36**, 21 (1969).

[57] A. Dalal and M. K. Das, Numer. Heat Tr. Part A: Applic. **49**, 301 (2006).

[58] S. M. Aminossadati and B. Ghasemi, Eur. J. Mech. B-Fluid. **28**, 630 (2009).

[59] J. M. Lopez and F. Marques, J. Fluid Mech. **736**, 616 (2013).